RSC Advances

PAPER

View Article Online
View Journal | View Issue

Cite this: *RSC Adv.*, 2020, **10**, 20713

Bismuth–iron-based precursor: preparation, phase composition, and two methods of thermal treatment†

Yunpeng Liu,[ab] Hao Wang,[ab] Lixiong Qian,[ab] Xiaoyi Zhao,[ab] Lei Yao,[a] Jiayi Wang,[a] Xueqing Xing,[a] Guang Mo,[a] Zhongjun Chen[a] and Zhonghua Wu *[ab]

Bismuth ferrite ($BiFeO_3$) is a promising Bi-based perovskite-type material, which is multiferroic due to the coexistence of anti-ferromagnetism and ferroelectricity. During the preparation of pure $BiFeO_3$ nanoparticles, however, the phase structures and species of bismuth–iron-based precursor (BFOH) were still unclear, and so related precursors were prepared. X-ray diffraction, Raman, Fourier transform infrared, and X-ray absorption near-edge structure techniques were used to probe the phase structure and species of the precursors. It was found that the precursor BFOH is composed of $Bi_6O_6(NO_3)_4(OH)_2{\cdot}2H_2O$, $Bi_6O_5(NO_3)_5(OH)_3{\cdot}3H_2O$, $Fe(OH)_3$, and α-Bi_2O_3. Calcination treatment and hydrothermal synthesis were used to prepare the pure $BiFeO_3$ phase from the precursor BFOH. The calcination temperature was optimized as 400 °C for preparation of the pure $BiFeO_3$ phase. Meanwhile, hydrothermal conditions for the synthesis of the pure $BiFeO_3$ phase were also optimized as follows: the reaction solution was the mixture solution of $Bi(NO_3)_3{\cdot}5H_2O$ and $Fe(NO_3)_3{\cdot}9H_2O$ with cetyltrimethyl ammonium bromide (CTAB) as the surfactant and KOH as the mineralizer; the hydrothermal synthesis was performed at 180 °C for 48 h; the concentration of KOH should be at least 3 M; and the surfactant CTAB can be used to regulate the morphology of the as-prepared $BiFeO_3$ nanoparticles. From the point of view of the microstructure, $BiFeO_3$ nanoparticles prepared by calcination or hydrothermal methods have no notable differences. A formation mechanism from the precursor BFOH to the $BiFeO_3$ product is proposed. By providing an understanding of the precursors, this work is very helpful in the synthesis of bismuth–iron-based nanoparticles.

Received 8th January 2020
Accepted 2nd May 2020

DOI: 10.1039/d0ra00177e

rsc.li/rsc-advances

1. Introduction

Magnetic and ferroelectric materials, as conventional research subjects, have a wide and important range of applications[1] in the field of electrical and sensor devices. Only a few materials exhibit both ferroelectric and magnetic polarizations,[2] and these are called multiferroic. Bismuth ferrite ($BiFeO_3$) is currently one[3] of the most studied multiferroic materials due to its promising applications at room temperature. $BiFeO_3$ shows a rhombohedrically distorted perovskite structure[4] with space group *R*3*c* at room temperature and atmospheric pressure. Its cell parameters are $a_{rh} = b_{rh} = c_{rh} = 3.965$ Å, and $\alpha_{rh} = \beta_{rh} = \gamma_{rh} = 89.3°$. In addition, the $BiFeO_3$ structure is also frequently described with a hexagonal unit cell,[3] in which $a_{hex} = b_{hex} = 5.58$ Å, $c_{hex} = 13.90$ Å, $\alpha_{hex} = \beta_{hex} = 90°$, and $\gamma_{hex} = 120°$. The ferroelectricity of $BiFeO_3$ originates from the stereochemically active lone-pair orbital[5] of the bismuth ions, which are largely displaced with respect to the octahedra and generate spontaneous polarization along the [111] axis of the rhombohedral unit cell. Furthermore, $BiFeO_3$ is a G-type anti-ferromagnet[6] in which all neighboring magnetic spins are oriented anti-parallel to each other, and the $BiFeO_3$ structure presents spin canting, which results in a weak magnetic moment in the unit cell according to the Dzyaloshinskii–Moriya interaction[7] due to the oxygen octahedral distortion. Typically, its ferroelectric Curie temperature (T_C) is about 830 °C, and the anti-ferromagnetic Neel temperature[8] (T_N) is about 370 °C.

In the past decade, $BiFeO_3$ nanoparticles (NPs) with different morphologies have been prepared, including nanospheres,[9] micro[10]/nanorods,[11] nanowires,[12–14] nanotubes,[15] and micro[16]/nanoplates.[17] Among the many synthesis methods for $BiFeO_3$ NPs, the hydrothermal method[11,14,18–27] is the most widely accepted and used. In addition, V. A. Reddy *et al.*[28] prepared nano-crystalline $BiFeO_3$ samples using the spray pyrolysis method. Nandini Das *et al.*[29] synthesized nano-sized bismuth ferrite powder through sonochemical and microemulsion techniques. H. Ke,[30] M. Y. Shami[31] and H. Shokrollahi[32] *et al.*

[a]*Institute of High Energy Physics, Chinese Academy of Sciences, Beijing 100049, China. E-mail: wuzh@ihep.ac.cn; liuyunpeng@ihep.ac.cn; Tel: +86-10-88235982*

[b]*University of Chinese Academy of Sciences, Chinese Academy of Sciences, Beijing 100049, China*

† Electronic supplementary information (ESI) available. See DOI: 10.1039/d0ra00177e

obtained nano-sized $BiFeO_3$ powders by using a chemical co-precipitation method. S. Ghosh *et al.*[33] produced bismuth ferrite products by utilizing the solid-state reaction between Bi_2O_3 and Fe_2O_3. N. A. Lomanova *et al.*[34] investigated the influence of synthesis temperature on the formation of $BiFeO_3$ NPs. C. Paraschiv *et al.*[35] obtained nano-sized $BiFeO_3$ by the combustion of $Fe(NO_3)_3 \cdot 9H_2O/Bi(NO_3)_3 \cdot 5H_2O$/glycine or urea systems. For all these methods, complicated synthesis steps are involved. Even for calcination and hydrothermal methods, many different types of starting materials, surfactants, or fuels are needed. To our knowledge, the phase structures and compositions of the precursors used in preparing $BiFeO_3$, which are very important for the synthesis of $BiFeO_3$ and its related Bi-based nanomaterials, are rarely studied. The formation processes for the precursors have puzzled researchers for a long time. In addition, impurity phases, such as Bi_2O_3, $Bi_{25}FeO_{40}$, and $Bi_2Fe_4O_9$, are easily produced during the preparation[4,23] of $BiFeO_3$ if the reaction conditions are not controlled properly. How to prepare pure $BiFeO_3$ product is also an important issue.

In this paper, the bismuth–iron-based precursor (BFOH) and other related precursors are prepared at room temperature. X-ray diffraction (XRD), Raman, Fourier transform infrared (FTIR), and X-ray absorption near-edge structure (XANES) spectroscopies are used to investigate the phase structures and compositions of the precursor BFOH for calcination and hydrothermal methods. The influence of synthetic conditions on the final products are systematically investigated, including reaction time, mineralizer concentration, the type and amount of surfactant in the hydrothermal synthesis, as well as the calcination temperature in the calcination synthesis. The optimal conditions to form pure $BiFeO_3$ product using calcination synthesis or hydrothermal synthesis are described.

2. Experimental details

2.1 Materials

The reagents, including bismuth nitrate pentahydrate ($Bi(NO_3)_3 \cdot 5H_2O$, abbreviated as BNO), iron nitrate nonahydrate ($Fe(NO_3)_3 \cdot 9H_2O$, abbreviated as FNO), cetyltrimethyl ammonium bromide ($C_{16}H_{33}(CH_3)_3NBr$, abbreviated as CTAB), polyvinyl pyrrolidone ($(C_6H_9NO)_n$, abbreviated as PVP), ethylenediaminetetraacetic acid ($C_{10}H_{16}N_2O_8$, abbreviated as EDTA), potassium hydroxide (KOH), and standard sample bismuth oxide (Bi_2O_3-std) were purchased from Aladdin Chemistry Co. Ltd. These reagents were analytical pure grade and were not further purified for use. In addition, absolute ethanol and distilled water were used in the sample preparation. A GSL-1600X/1400X double-temperature vacuum tube furnace was purchased from Hefei Kejing Material Technology Co. Ltd. The hydrothermal apparatus of a teflon-lined stainless steel autoclave was purchased from Anhui Kemi Machinery Technology Co. Ltd.

2.2 Preparation of precursors

In a typical synthesis process, BNO and FNO were used as metal sources and distilled water was used as solvent. First, 4 mmol of BNO and 4 mmol FNO were, respectively, dissolved in 20 ml of distilled water, then the two solutions were mixed to give 40 ml of solution. An aqueous solution of 3 M KOH (40 ml) was added dropwise into the mixture with vigorous stirring for 30 min, forming a homogeneous reddish-brown colloid. The resulting precipitate was collected after centrifuging the colloid. Finally, the precipitate was dried at 60 °C for 6 h. After grinding the dry precipitate, the bismuth–iron-based precursor powders were prepared and labeled as BFOH. With a similar synthesis process, precipitates were also obtained in the absence of FNO and BNO, respectively, and the two precipitates were labeled as BNO–KOH and FNO–KOH, respectively. In addition, the hydrolysate of BNO was also specifically obtained, and labeled as BNO–H_2O.

2.3 Calcination of BFOH

To investigate the phase transition process, the precursor BFOH was calcinated at temperatures of 25, 200, 300, 400, 500, and 600 °C, respectively, for 3 h in the GSL-1600X/1400X double-temperature vacuum tube furnace. After cooling the furnace to room temperature and grinding the calcination products into powders, the final powders were collected and labeled as BFOH-x, where x refers to the calcination temperature.

2.4 Hydrothermal treatment of BFOH

First, the as-prepared BFOH precursor was dispersed in 3 M KOH aqueous solution. After vigorously stirring for 20 min, the precursor solution was transferred into a 100 ml teflon-lined stainless steel autoclave and maintained at 180 °C for 48 h. Afterwards, the autoclave was cooled to room temperature and the hydrothermal precipitate was collected by centrifugation. After washing several times with distilled water and absolute ethanol to remove impurities as much as possible, the precipitate was dried at 80 °C for 4 h to form the final product, denoted as BFO. With a similar synthesis process as for the preparation of BFOH, CTAB as surfactant was added into the reaction solution, which was used to tune the morphologies of the final products. After hydrothermal treatment, the resulting products were also obtained after centrifuging and washing and were labeled as BFOC-y, here y represents the amount (0.1, 0.3, and 0.5 g) of CTAB in the preparation. The synthesis conditions and parameters for all the samples are summarized in Table 1.

2.5 Characterization

Powder XRD patterns were collected at the XRD station of beamline 4B9A at the Beijing Synchrotron Radiation Facility (BSRF), with incident X-ray energy of 8050 eV ($\lambda = 1.5402$ Å). Raman spectra were also collected with a Raman spectrometer (HORIBA, LabRAM HR Evolution). FTIR spectra were recorded on a Bruker TENSOR27 instrument equipped with a quartz sample holder with KBr windows. The X-ray absorption spectra for the Bi L_3-edge and Fe K-edge were measured at the X-ray absorption fine structure (XAFS) station of beamline 1W1B and the XRD station of beamline 4B9A of BSRF, respectively, in transmission mode. Scanning electron microscopy (SEM, HITACHI S-4800) and high-angle annular dark field scanning

Table 1 Synthesis details for all precursors and their corresponding products

Sample types	Starting materials	Synthesis conditions	Labels
Precursors	4 mmol BNO, 4 mmol FNO, deionized water, KOH (3 M)	Room temperature, mixing dropwise, and stirring	BFOH
	4 mmol BNO, deionized water, KOH (3 M)	Room temperature, mixing dropwise, and stirring	BNO–KOH
	4 mmol FNO, deionized water, KOH (3 M)	Room temperature, mixing dropwise, and stirring	FNO–KOH
	4 mmol BNO, deionized water	Room temperature, mixing, and stirring	BNO–H_2O
Calcined products	BFOH	Calcined at 200 °C for 3 h	BFOH-200 °C
		Calcined at 300 °C for 3 h	BFOH-300 °C
		Calcined at 400 °C for 3 h	BFOH-400 °C
		Calcined at 500 °C for 3 h	BFOH-500 °C
		Calcined at 600 °C for 3 h	BFOH-600 °C
Hydrothermal products	4 mmol BNO, 4 mmol FNO, deionized water, KOH (3 M)	Hydrothermal treatment at 180 °C for 48 h	BFO
	4 mmol BNO, 4 mmol FNO, deionized water, KOH (3 M), CTAB	Hydrothermal treatment at 180 °C for 48 h	BFOC-0.1 g BFOC-0.3 g BFOC-0.5 g

transmission electron microscopy (HAADF-STEM, FEI Titan G2 microscope, accelerating voltage: 300 kV, equipped with a probe spherical aberration corrector, enabling sub-angstrom imaging using HAADF-STEM detectors) were used to observe the morphologies of the samples. Thermogravimetric analysis (TGA) and differential scanning calorimetry (DSC) analysis were performed on a Mettler Toledo TGA/DSC1 STAR^e system. The samples were heated from ambient temperature to 1000 °C with a heating rate of 10 °C min^{-1} under N_2 flow.

3. Results and discussion

3.1 Phase structures of precursors

To judge the structure of precursor BFOH in the preparation of $BiFeO_3$, first the Raman and FTIR spectra of the four precursors BNO–KOH, BFOH, FNO–KOH, and BNO–H_2O were collected, as shown in Fig. 1. It can be seen that the Raman spectral characteristics of BFOH are very similar to those of BNO–H_2O and FNO–KOH within the Raman shift region from 224 to 430 cm^{-1}. This result could imply that the Bi–O–Bi and Bi–OH bond vibrations,[36] as in BNO–H_2O, as well as the Fe–O–Fe and Fe–OH bonds vibrations,[37] as in FNO–KOH, are combined and included in the BFOH precursor. Similarly, the Raman spectral characteristics of BFOH in the range 40–165 cm^{-1}, as shown in Fig. 1(a), can also be attributed to a combination of the Bi–O bond vibrations[36] in BNO–H_2O and the Fe–O bond vibrations[37] in FNO–KOH, and even the Bi–Bi bond vibrations[38] in BNO–KOH. Several major absorption band features of the FTIR spectrum of the BFOH precursor are visible, as shown in Fig. 1(b). The feature at 538 cm^{-1} corresponds to the Bi–O vibrations[39,40] of the BiO_6 coordination polyhedron. However, the relatively wide feature near 538 cm^{-1} in BFOH seem to be a joint contribution of the 565 cm^{-1} feature in BNO–H_2O and the 642 cm^{-1} feature in FNO–KOH. The features around 849, 1036, 1325, and 1487 cm^{-1} correspond to the symmetric and asymmetric stretching vibrations[41–43] of the nitro group, with

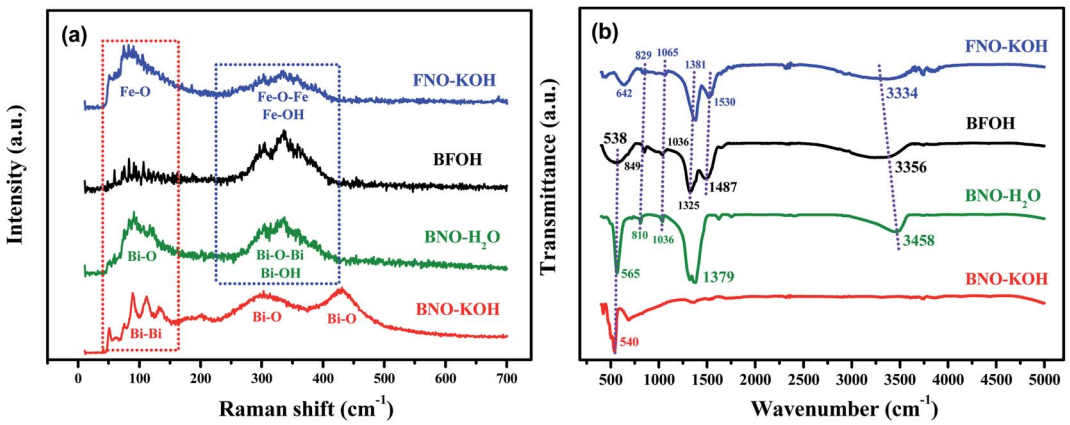

Fig. 1 (a) Raman spectra and (b) FTIR spectra of the four as-prepared precursors (BFOH, BNO–H_2O, FNO–KOH, and BNO–KOH).

the two features at 849 and 1036 cm^{-1} also found in the FTIR spectra of FNO–KOH and BNO–H_2O at the same position. The other two features, at 1325 and 1487 cm^{-1}, confirm that BFOH is more similar to FNO–KOH than to BNO–H_2O. The feature at 3356 cm^{-1} corresponds to the vibration mode of the water molecule[44] or hydroxyl (–OH) group[45] stretching vibrations. Similar features can be also found in the FTIR spectra of FNO–KOH and BNO–H_2O. Generally, these Raman and FTIR spectra imply that the BFOH precursor has some similar vibration modes or molecular groups as the precursors FNO–KOH and BNO–H_2O.

To further verify the composition and structure of the precursors, transmission XAFS spectra of the four precursors, BNO, and FNO were collected. The normalized Bi L_3-edge XAFS spectra of BFOH, BNO–H_2O, BNO–KOH, BNO and the normalized Fe K-edge XAFS spectra of BFOH, FNO–KOH, and FNO are shown in Fig. S1 (ESI†). The Fe K-edge XAFS spectrum of BFOH is almost the same as that for FNO–KOH. However, the Bi L_3-edge XAFS spectrum of BFOH is not completely overlapping with that of BNO–KOH. This result means that the near-neighbor structures around the Fe center are almost the same in BFOH and FNO–KOH, but that the near-neighbor structures around the Bi center are different from those of BNO–KOH. To refine the fraction of each species, the linear combination fitting (LCF) method was used to quantify the species in the precursor BFOH performing the ATHENA program.[46] Here, LCF was performed for the normalized XANES spectra over the range 13 399 to 13 519 eV (Bi L_3-edge) or from 7092 to 7212 eV (Fe K-edge), respectively. In the fitting of the Bi L_3-edge XANES spectrum, BNO–KOH, BNO–H_2O, and BNO were used as the reference species. And, FNO–KOH and FNO were used as the reference species in the fitting of Fe K-edge XANES spectrum. The XANES components and the fitting results are shown in Fig. 2. From the Bi L_3-edge spectrum, as shown in Fig. 2(a), the fitting components of BFOH are BNO–KOH (48.5%) and BNO–H_2O (50.1%), as well as extremely small amounts of BNO (about 1.4%). From the Fe K-edge spectrum, as shown in Fig. 2(b), the fitting result indicates that BFOH contains only the species of FNO–KOH. These XANES results demonstrate that the main components in the precursor BFOH could be the species BNO–KOH, BNO–H_2O and FNO–KOH, which is consistent with the results of Raman and FTIR.

Based on the Raman, FTIR, and XAFS results, the phase of precursor BFOH is still not completely determined. Therefore, the XRD technique was further used to analyze the phase content of the precursor BFOH. First, the XRD pattern of BNO–KOH is shown in Fig. 3(a), which can be attributed to a monoclinic bismite (Bi_2O_3) structure with space group $P2_1/c$ as indicated by the PDF code 41-1449, where $a = 5.850$, $b = 8.170$, and $c = 7.512$ Å, $\alpha = \gamma = 90°$, $\beta = 112.977°$. For comparison, the XRD pattern (Fig. S2, ESI†) of another purchased bismuth oxide (marked as Bi_2O_3-std) was also measured and can be attributed to the space group $P\bar{4}\,2_1/c$ as indicated by the PDF code 27-0050, where $a = 7.742$, $b = 7.742$, and $c = 5.631$ Å, $\alpha = \beta = \gamma = 90°$. Although both the precursor BNO–KOH and the purchased standard bismuth oxide sample have the same chemical formula (Bi_2O_3) and very similar molecule vibration modes (Fig. S3, ESI†), their crystal structures (Fig. S2, ESI†) and colors (Fig. S4, ESI†) are different. Actually, the precursor BNO–KOH and the purchased bismuth oxide are the so-called α-Bi_2O_3 (ref. 47) and β-Bi_2O_3,[48] respectively. Therefore, the following reaction occurred as KOH was added dropwise into the BNO aqueous solution:

$$2Bi(NO_3)_3\cdot 5H_2O + 6KOH + H_2O \rightarrow \alpha\text{-}Bi_2O_3\downarrow + 6KNO_3 + 14H_2O \quad (1)$$

Here, the reaction precipitate between BNO and KOH is α-Bi_2O_3, instead of $Bi(OH)_3$, as previously reported in the literature.[49]

Second, the XRD pattern of BNO–H_2O is shown in Fig. 3(b). It is well known that bismuth nitrate (BNO)[50,51] is easy to hydrolyze after dissolving it in distilled water, which seriously impedes the synthesis of pure $BiFeO_3$ and the monodispersity of the product particles. In our previous work, monodisperse and pure

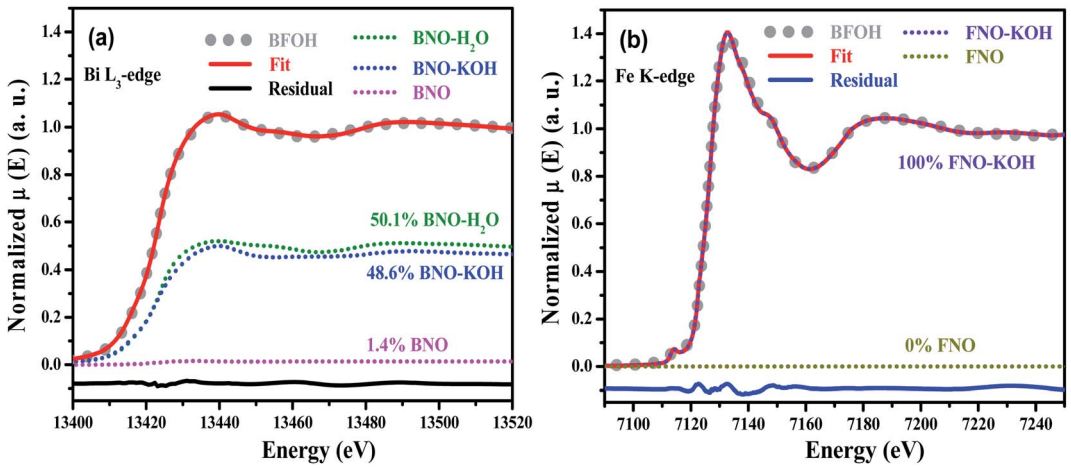

Fig. 2 Normalized LCF XANES spectra of (a) Bi L_3-edge and (b) Fe K-edge for the precursor BFOH. The as-prepared BNO–H_2O, BNO–KOH, and BNO were used as the standard species for the Bi L_3-edge spectrum, and FNO–KOH and FNO were used as the standard species for the Fe K-edge spectrum.

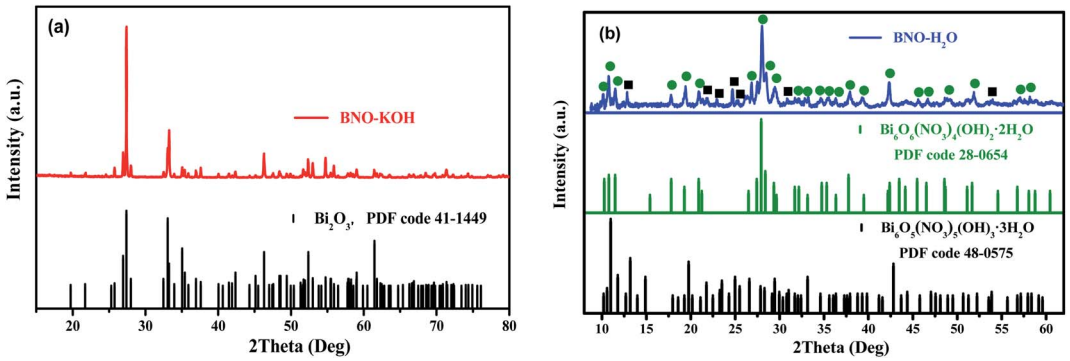

Fig. 3 XRD patterns of the as-prepared precursors (a) BNO–KOH and (b) BNO–H_2O. The relevant XRD patterns of α-Bi_2O_3, $Bi_6O_5(NO_3)_5(OH)_3\cdot 3H_2O$ and $Bi_6O_6(NO_3)_4(OH)_2\cdot 2H_2O$ are also presented.

bismuth nanoparticles (Bi NPs)[52] were successfully prepared by dissolving BNO in ethylene glycol (EG). Although distilled water is still the best solvent in the synthesis of $BiFeO_3$, the phase structure of the BNO hydrolysate (BNO–H_2O) puzzles many researchers. X. Wang[9] and Q. Wang[53] *et al.* reported that bismuth subnitrate ($BiONO_3$) can be prepared by dispersing BNO in distilled water, based on the following reaction:

$$2Bi(NO_3)_3\cdot 5H_2O \rightarrow 2BiONO_3\downarrow + 4HNO_3 + 8H_2O. \quad (2)$$

Y. He *et al.* reported[54] that the hydrolysate of BNO is $Bi_6O_5(NO_3)_5(OH)_3\cdot 3H_2O$, according to the following hydrolysis equation:

$$6Bi(NO_3)_3\cdot 5H_2O \rightarrow Bi_6O_5(NO_3)_5(OH)_3\cdot 3H_2O\downarrow + 13HNO_3 + 19H_2O. \quad (3)$$

In this work, the hydrolysate of BNO (BNO–H_2O powder) was also prepared. Evidently, its powder color (Fig. S5, ESI†), XRD pattern (Fig. S6(a), ESI†), and molecular vibration (Fig. S6(b), ESI†) are different from the starting material BNO. By carefully comparing its XRD pattern with some known species and structures, it can be determined that the precursor BNO–H_2O can be attributed to a mixture consisting of $Bi_6O_6(NO_3)_4(OH)_2\cdot 2H_2O$ (PDF code 28-0654) and $Bi_6O_5(NO_3)_5(OH)_3\cdot 3H_2O$ (PDF code 48-0575) as shown in Fig. 3(b). A possible reaction process to form the mixture phases can be described as below:

$$12Bi(NO_3)_3\cdot 5H_2O \rightarrow Bi_6O_6(NO_3)_4(OH)_2\cdot 2H_2O + Bi_6O_5(NO_3)_5(OH)_3\cdot 3H_2O + 27HNO_3 + 39H_2O. \quad (4)$$

To figure out the species and structure of the precursor BFOH, XRD patterns of the four precursors BFOH, BNO–KOH, FNO–KOH, and BNO–H_2O are compared in Fig. 4. Obviously, there is an amorphous bulge located at 20–40° on the XRD pattern of the precursor BFOH, and some sharp diffraction peaks superimposed on the amorphous background. For each diffraction peak of BFOH, a corresponding diffraction peak can always be found from the three XRD patterns of BNO–KOH, FNO–KOH, and BNO–H_2O. This result implies that the precursor BFOH is a mixture containing these precursors of BNO–KOH, FNO–KOH and BNO–H_2O. The color changes of the BFOH, BNO–KOH, FNO–KOH, and BNO–H_2O powders (Fig. S7, ESI†) also support this result. We note that the diffraction intensity for FNO–KOH is relatively weak. Several weak diffraction peaks in the XRD pattern of FNO–KOH mean that most of the precursor FNO–KOH forms noncrystalline ferrite and a small fraction forms a crystalline phase. The reflection at 23.5° in the XRD pattern of FNO–KOH can only be attributed to diffraction from crystalline $Fe(OH)_3$ (PDF code 46-1436 (Fig. S8, ESI†)). Previous research[21] claimed that the precursor FNO–KOH was amorphous $Fe(OH)_3$, but in this work at least some precipitates of $Fe(OH)_3$ were crystalline. The formation of $Fe(OH)_3$ in the solution reaction can be described as follows:

$$Fe(NO_3)_3\cdot 9H_2O + 3KOH \rightarrow Fe(OH)_3\downarrow + 3KNO_3 + 9H_2O. \quad (5)$$

On the basis of the above discussion, it can be concluded that the amorphous bulge on the XRD pattern of BFOH may come from the amorphous component of FNO–KOH. The precursor BFOH may be a mixture containing the amorphous

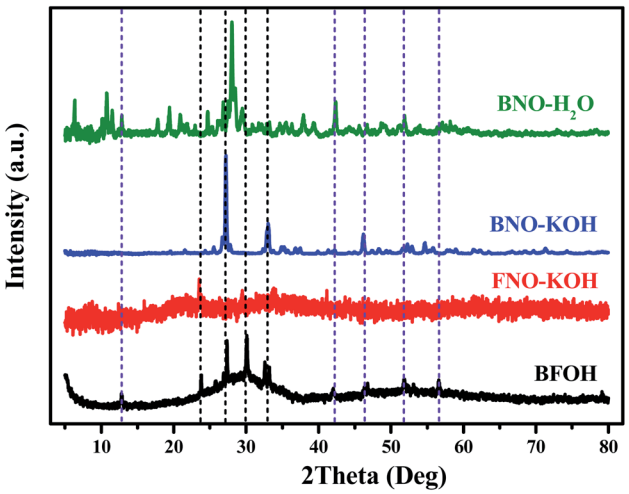

Fig. 4 XRD patterns of the four as-prepared precursors (BFOH, FNO–KOH, BNO–KOH, and BNO–H_2O).

component, $Fe(OH)_3$, and α-Bi_2O_3, $Bi_6O_6(NO_3)_4(OH)_2 \cdot 2H_2O$, and $Bi_6O_5(NO_3)_5(OH)_3 \cdot 3H_2O$.

3.2 Calcination of BFOH

To investigate the changes of structure and phase, the precursor BFOH was further calcined at different temperatures from 25 to 600 °C. The calcined samples are marked as BFOH-*x*, where *x* denotes the calcined temperature. Their XRD patterns and FTIR spectra were collected as shown in Fig. 5(a) and (b), respectively. Comparatively speaking, the first three samples (BFOH, BFOH-200 °C, and BFOH-300 °C) have negligible diffraction intensities compared with the other samples. Obviously, the noncrystalline phase is the main component of the first three samples. When the calcined temperature was 400 °C, significant diffraction peaks can be observed from the corresponding XRD pattern (BFOH-400 °C) and can be indexed as a hexagonal $BiFeO_3$ phase with space group *R3c*, as indicated by JCPDS card no. 86-1518, where $a = b = 5.587$ Å, $c = 13.867$ Å, $\alpha = \beta = 90°$, $\gamma = 120°$. The formation of $BiFeO_3$ can be described by the following reaction:

$$\alpha\text{-}Bi_2O_3 + 2Fe(OH)_3 \rightarrow 2BiFeO_3 + 3H_2O. \quad (6)$$

When the calcined temperature was further increased to 500 °C, the diffraction intensities of the hexagonal $BiFeO_3$ phase increased further, and several other weak peaks emerged at the same time. The diffraction-intensity enhancement of the hexagonal phase means that the BFOH-500 °C sample has better crystallinity and larger particle size for the $BiFeO_3$ phase than the BFOH-400 °C sample. These newly formed weak peaks can be ascribed to the diffraction of Bi_2O_3, $Bi_{25}FeO_{40}$, and $Bi_2Fe_4O_9$. This result demonstrates that a few impurity phases appear in the sample with grain growth of $BiFeO_3$ hexagonal phase. When the calcined temperature rose further to 600 °C, the diffraction intensity of the $BiFeO_3$ hexagonal phase was almost unchanged, but those of the impurity phases Bi_2O_3, $Bi_{25}FeO_{40}$, and $Bi_2Fe_4O_9$ clearly increased. In fact, the components of $Bi_6O_6(NO_3)_4(OH)_2 \cdot 2H_2O$ and $Bi_6O_5(NO_3)_5(OH)_3 \cdot 3H_2O$ in the precursor BFOH have been decomposed at calcined temperature of 500–600 °C as follows:

$$Bi_6O_6(NO_3)_4(OH)_2 \cdot 2H_2O + O_2 \rightarrow 3Bi_2O_3 + 3H_2O + 2N_2O_5. \quad (7)$$

$$2Bi_6O_5(NO_3)_5(OH)_3 \cdot 3H_2O \rightarrow 6Bi_2O_3 + 9H_2O + 5N_2O_5. \quad (8)$$

$$26Bi_2O_3 + 6Fe(OH)_3 \rightarrow 2Bi_{25}FeO_{40} + Bi_2Fe_4O_9 + 9H_2O. \quad (9)$$

It is the reactions in eqn (7)–(9) that lead the appearance of the impurity phases Bi_2O_3, $Bi_{25}FeO_{40}$, and $Bi_2Fe_4O_9$.

The FTIR spectra of the calcined samples are shown in Fig. 5(b). Similarly, the first three calcined samples (BFOH, BFOH-200 °C, and BFOH-300 °C) have almost the same spectral features, which can be ascribed to vibrations of the Bi–O bond[39,40] (not Fe–O[55]), nitro group,[41–43] water molecule,[44] and hydroxyl group.[45] The main differences between the three samples focus on that fact the vibration of the water molecules fades away, while the vibration of the hydroxyl group gradually increases with increase in calcination temperature. This result means that water in the sample was gradually evaporated and the amorphous component was gradually crystallized. As the calcined temperature increased to 400 and 500 °C, FTIR spectral features of the two samples were already very similar to those[55] of $BiFeO_3$. The appearance of Fe–O stretching vibration modes and O–Fe–O and Fe–O–Fe bending vibration modes corresponds to the formation[55] of the $BiFeO_3$ phase, in which the bending vibration modes come from the tetrahedral sites.[56,57] Because of the increase in content of the impurity phases Bi_2O_3, $Bi_{25}FeO_{40}$, and $Bi_2Fe_4O_9$ at the calcined temperature of 600 °C, the FTIR spectrum of BFOH-600 °C differs slightly from those of BFOH-400 °C and BFOH-500 °C.

To further confirm the structures and morphologies of the calcination samples BFOH-400 °C and BFOH-500 °C, SEM, TEM, and high-resolution TEM (HRTEM) images were recorded and are shown in Fig. 6. The SEM images indicate that both samples have a morphology of particle agglomeration. However, the particle shape for BFOH-400 °C is irregular and the particle size is small (Fig. 6(a)), while the particle shape for BFOH-500 °C

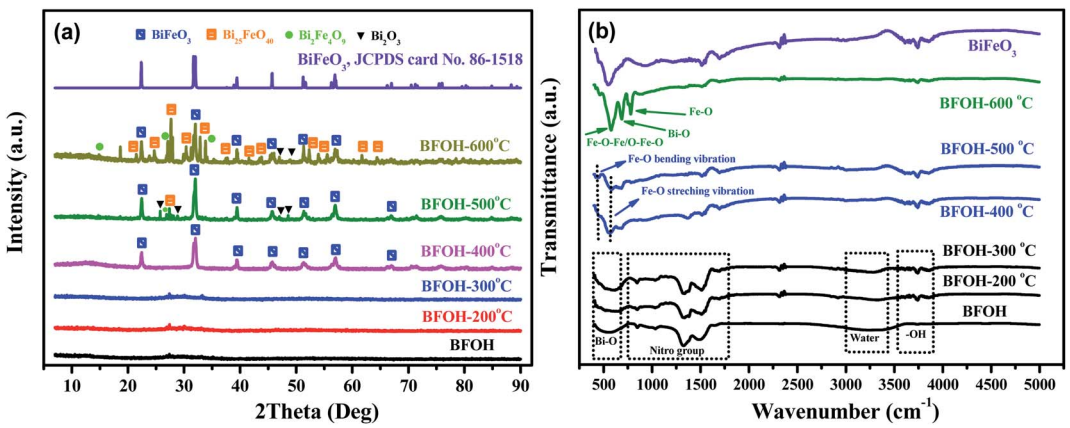

Fig. 5 XRD patterns (a) and FTIR spectra (b) of the as-prepared samples BFOH, BFOH-200 °C, BFOH-300 °C, BFOH-400 °C, BFOH-500 °C, and BFOH-600 °C.

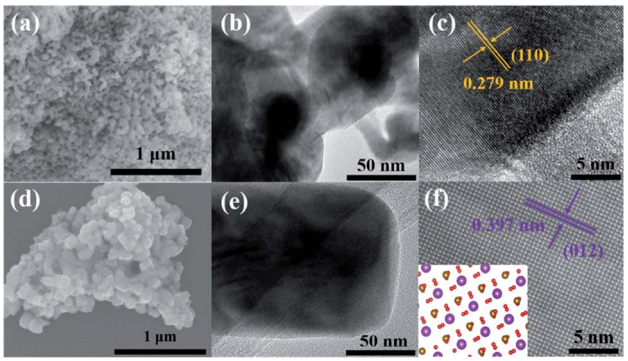

Fig. 6 SEM (a and d), TEM (b and e), and HRTEM (c and f) images of the calcination samples BFOH-400 °C (a–c) and BFOH-500 °C (d–f).

is approximately orthogonal hexahedron and the particle size is large (Fig. 6(d)). TEM images further identified these particle shapes, as well as the particle sizes. It was the increase in calcination temperature from 400 to 500 °C that improved the growth rate[58,59,61] and activated growth[60] of $BiFeO_3$ particles, resulting in the particle size increasing from 50 nm (Fig. 6(b)) to 100 nm (Fig. 6(e)). The HRTEM images of BFOH-400 °C and BFOH-500 °C are shown in Fig. 6(c) and (f). The clear lattice fringes illustrate the crystallization characteristics of the two samples. In particular, the orthogonal fringes in Fig. 6(f) show clearly the $(100)_c$ crystal plane characteristics of the $BiFeO_3$ pseudo-cubic phase, or the projection characteristics along the $[42\bar{1}]_h$ direction of the $BiFeO_3$ hexagonal phase, as confirmed by the inset in Fig. 6(f). The fringe spacings of 0.279 or 0.397 nm correspond to the *d*-spacing of the (110) or (012) planes in crystalline $BiFeO_3$, which again confirms that the dominant crystalline phase is the $BiFeO_3$ nanocrystals in the BFOH-400 °C and BFOH-500 °C samples.

The element types and distributions in the samples BFOH-400 °C and BFOH-500 °C were also recorded, as shown in the mapping pictures (Fig. S9, ESI†). The results demonstrate that the three elements (Bi, Fe, O) distributed homogeneously in the two samples BFOH-400 °C and BFOH-500 °C. In addition, the thermostability of the BFOH-400 °C sample (crystalline $BiFeO_3$ phase) was also examined by thermal analysis. Fig. 7(a) shows the DSC curve of the BFOH-400 °C sample, where only two endothermic features are distinguishable. The endothermic peak[8] around 828 °C was claimed to correspond to the phase transformation from ferroelectric to paraelectric, with the endothermic peak[31,62] at 957 °C corresponding to the melting point of $BiFeO_3$. These results excluded the possibility of thermal decomposition of $BiFeO_3$ in the temperature range of 500–600 °C. Thermal analysis was also performed for the as-prepared BFOH precursor and the corresponding TGA/DSC curves are shown in Fig. 7(b). It can be seen that the BFOH precursor experiences a significant loss of mass from room temperature to 400 °C. Afterwards, the mass loss of the sample is negligible. In this work, the calcination temperature of 400 °C is a key point to form the $BiFeO_3$ phase. On the whole, there are no mutational and remarkable endothermic or exothermic reactions occurring below 900 °C. Several weak endothermic peaks can be found around 459 °C, 665 °C, and 708 °C. The weak endothermic peak at 459 °C could correspond to the decomposition of the two mesophases $Bi_6O_6(NO_3)_4(OH)_2 \cdot 2H_2O$ and $Bi_6O_5(NO_3)_5(OH)_3 \cdot 3H_2O$ in the precursor BFOH. The origin of the other two endothermic peaks, at 665 °C and 708 °C, are still unclear. Generally, the calcination process has hardly any influence on the precursor BFOH when the calcined temperature is lower than 300 °C. At 400 °C, only the $BiFeO_3$ crystalline phase can be formed. Impurity phases Bi_2O_3, $Bi_{25}FeO_{40}$, and $Bi_2Fe_4O_9$ appear at higher calcination temperatures (500–600 °C).

3.3 Hydrothermal synthesis optimization

To optimize the hydrothermal synthesis process of $BiFeO_3$, a series of reaction conditions, such as reaction time, type, and amount of surfactant, and concentration of KOH (as mineralizer) have been investigated. All the hydrothermal synthesis details are listed in Table 2. The hydrothermal reaction temperature was chosen as 180 °C, as in a typical hydrothermal synthesis[14,24] of $BiFeO_3$. Surfactants can be used to modify the morphology[63] of nanoparticles and act as structure-directing reagents[64] in forming $BiFeO_3$ nanoparticles. In this study, the surfactants PVP, EDTA, and CTAB were compared for the

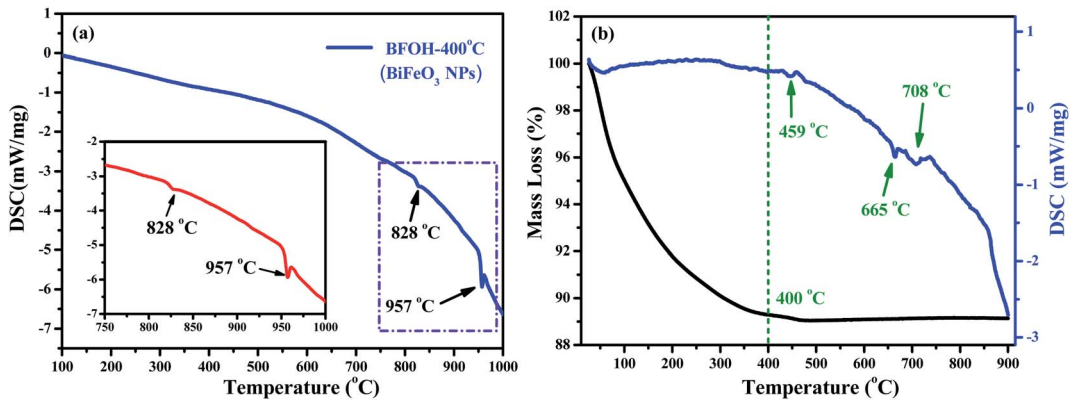

Fig. 7 (a) DSC curve of the BFOH-400 °C powder. Inset shows the enlarged view of the selected area. (b) TGA/DSC curves of the as-prepared BFOH precursor.

Table 2 Synthesis details of the corresponding hydrothermal products

Starting materials	Synthesis conditions	Labels
4 mmol BNO, 4 mmol FNO, deionized water, KOH (3 M)	Hydrothermal treatment at 180 °C for 24 h	BFO-24 h
	Hydrothermal treatment at 180 °C for 48 h	BFO-48 h
	Hydrothermal treatment at 180 °C for 72 h	BFO-72 h
4 mmol BNO, 4 mmol FNO, deionized water, KOH (3 M), 0.5 g PVP	Hydrothermal treatment at 180 °C for 48 h	BFO–PVP
4 mmol BNO, 4 mmol FNO, deionized water, KOH (3 M), 0.5 g EDTA	Hydrothermal treatment at 180 °C for 48 h	BFO–EDTA
4 mmol BNO, 4 mmol FNO, deionized water, KOH (3 M), 0.5 g CTAB	Hydrothermal treatment at 180 °C for 48 h	BFO–CTAB
4 mmol BNO, 4 mmol FNO, deionized water, KOH (1 M)	Hydrothermal treatment at 180 °C for 48 h	BFO-1 M
4 mmol BNO, 4 mmol FNO, deionized water, KOH (2 M)	Hydrothermal treatment at 180 °C for 48 h	BFO-2 M
4 mmol BNO, 4 mmol FNO, deionized water, KOH (3 M)	Hydrothermal treatment at 180 °C for 48 h	BFO-3 M
4 mmol BNO, 4 mmol FNO, deionized water, KOH (4 M)	Hydrothermal treatment at 180 °C for 48 h	BFO-4 M
4 mmol BNO, 4 mmol FNO, deionized water, KOH (5 M)	Hydrothermal treatment at 180 °C for 48 h	BFO-5 M

optimum synthesis of $BiFeO_3$. After a series of experimental explorations of the hydrothermal processes (Fig. S10–S12, ESI†), the optimal hydrothermal conditions to synthesize pure $BiFeO_3$ phase can be summarized as follows: the suitable reaction time is 48 h; the preferred surfactant is CTAB; and the necessary concentration of KOH is at least 3 M. The influence of the amount of CTAB on the morphology of the final products was also investigated. Fig. 8(a) shows the XRD patterns of three samples (BFOC-0.1 g, BFOC-0.3 g, and BFOC-0.5 g) with different amounts of CTAB. The three XRD patterns can all be indexed as a pure $BiFeO_3$ phase. The main difference is that the intensities of the (012) and (104) reflections increase with increasing amount of CTAB, as shown in Fig. 8(b). This result indicates that the [012] and [104] directions are the preferential growth directions of $BiFeO_3$ grains in the presence of CTAB in the hydrothermal solution. Fig. 9 shows the SEM images of samples BFOC-0.1 g, BFOC-0.3 g, and BFOC-0.5 g ((a)–(c)), the TEM images of sheet-like and flat-cylindrical particles ((d)–(f)), and the HRTEM images of BFOC-0.1 g, BFOC-0.3 g, and BFOC-0.5 g ((g)–(i)), respectively. Obviously, the particles with low CTAB content (BFOC-0.1 g) are sheet-like. With the amount of CTAB increasing to 0.3 g, the particles (BFOC-0.3 g) are approximately flat-cylindrical. When the amount of CTAB increases to 0.5 g, these cylindrical particles (BFOC-0.5 g) grow further, especially in height. The sheet-like or flat-cylindrical shapes of the particles can be further confirmed by the TEM images.

To acquire more structural details, HRTEM images of the three samples are also shown in Fig. 9(g)–(i). In all three HRTEM images, the lattice fringes with spacing of about 0.28 nm are always visible, which corresponds to the spacing of the (110) planes in the $BiFeO_3$ crystal. This result implies that the surface of the sheet-like particles, or the top and bottom surfaces of the flat-cylindrical particles, are the (001) plane. Indeed, an increase in the thickness of the flat-cylindrical particles relative to the sheet-like particles implies an increase in the number of (001) planes. It is the increment in particle thickness along the [001] direction that results in the increase in the number of (012) and (104) planes and enhancement of the (012) and (104) reflections. While the relative change in diameter of the flat-cylindrical particles is small. This means that the efficient volume for the (110) reflection is almost unchanged. Therefore, the intensity of the (110) reflection does not show an obvious change, as in Fig. 8(b). A set of fringes with spacing of about 0.55 nm can also be observed, as shown in Fig. 9(i). The 0.55 nm spacing corresponds to interplanar spacing of the (100) or (010)

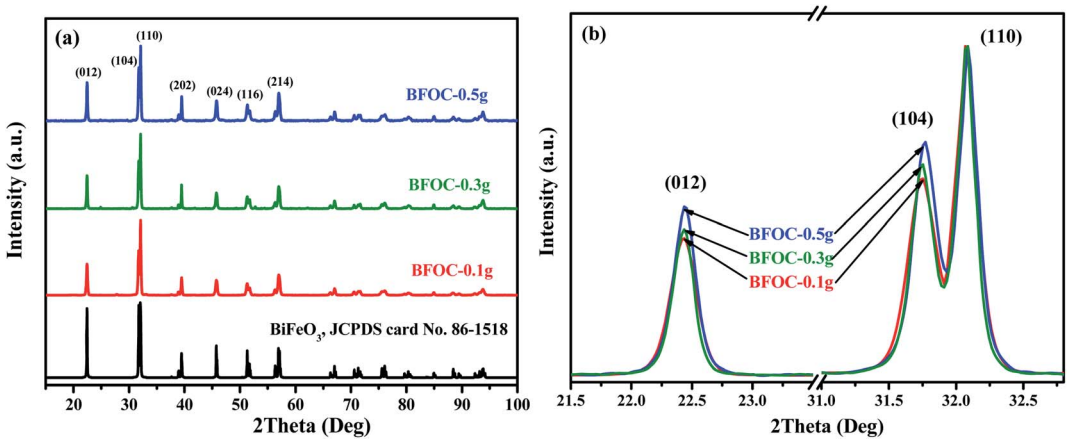

Fig. 8 (a) XRD patterns of the as-prepared BFOC-0.1 g, BFOC-0.3 g, and BFOC-0.5 g. (b) Diffraction peak comparison of (012) and (104) reflections.

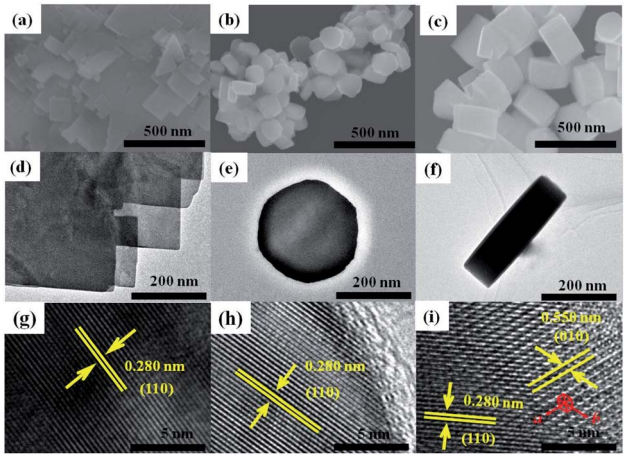

Fig. 9 SEM images of the as-prepared samples (a) BFOC-0.1 g, (b) BFOC-0.3 g, and (c) BFOC-0.5 g. TEM images of (d) sheet-like particles as well as (e) bottom view and (f) side view of flat-cylindrical particles. HRTEM images of samples (g) BFOC-0.1 g, (h) BFOC-0.3 g, and (i) BFOC-0.5 g.

planes in the $BiFeO_3$ crystal. By carefully observing the HRTEM image in Fig. 9(i), a hexagonal atomic arrangement is distinguishable. This result again confirms that the fringes with spacings of 0.28 nm and 0.55 nm are from the (110) and (010) planes, respectively, of the $BiFeO_3$ crystal. All of these findings identify that the exposed plane of the sheet-like particles, or the top and bottom surfaces of the flat-cylindrical particles, are the (001) plane of the $BiFeO_3$ crystal, whereas previous work[64] suggested that the exposed surface of $BiFeO_3$ flat plates, which resembled hexagons, was the (104) facet.

Based on the above XRD, SEM and TEM results, it can be concluded that CTAB plays a regulating role in the aggregation and growth of $BiFeO_3$ NPs. When the amount of CTAB added into the hydrothermal solution was low, the influence of CTAB on the growth of $BiFeO_3$ particles was less. In this case, the $BiFeO_3$ particles had a sheet-like shape. As the amount of CTAB added to the hydrothermal solution increased, more CTAB molecules were absorbed onto the side faces of the hexagonal $BiFeO_3$ crystallite than onto the upper and lower surfaces, or the (001) plane. In this case, the higher coverage of CTAB molecules on the side faces of the $BiFeO_3$ crystallites further prevented or postponed crystal growth along the normal directions of the side faces. In other words, the [001] direction was a relatively easier growth direction, which meant that the $BiFeO_3$ flat-cylindrical particles grew faster in the direction of height than in the radial direction. The increase of the crystallite thickness along the [001] direction also increased the number of other (hkl) crystal planes with $l \neq 0$. As a result, the (012) and (104) planes exhibit more intense XRD peaks with increase in the amount of CTAB.

3.4 Method comparison of synthesized $BiFeO_3$

In this work, calcination (CC) and hydrothermal (HT) methods have been used to synthesize bismuth ferrite. Both methods were optimized to synthesize pure hexagonal $BiFeO_3$ phase. The

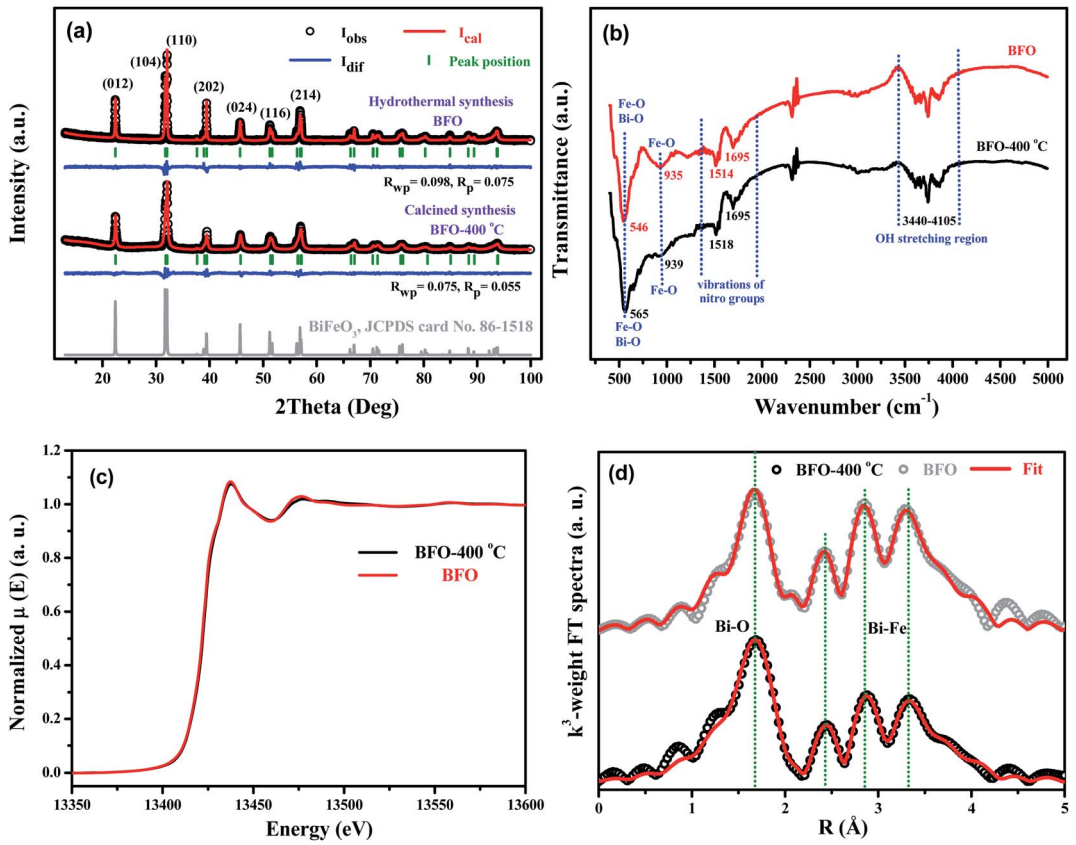

Fig. 10 (a) XRD patterns, (b) FTIR spectra, (c) Bi L_3-edgeXAFS spectra and (d) FT spectra of EXAFS oscillations $k^3\chi$ (k) for BFO-400 °C and BFO.

sample prepared by the calcination method is indicated as BFO-400 °C, while the sample prepared by the hydrothermal method is indicated as BFO. XRD, FTIR, and XAFS data for the two samples were collected for comparison. The XRD patterns shown in Fig. 10(a) verify that BFO and BFO-400 °C can be attributed to pure hexagonal $BiFeO_3$ phases. The GSAS program[65] was used to perform Rietveld refinement of the lattice parameters. For BFO-400 °C, $a_{CC} = b_{CC} = 5.577$ Å, $c_{CC} = 13.831$ Å and for BFO, $a_{HT} = b_{HT} = 5.581$ Å, $c_{HT} = 13.867$ Å. The unit cell is slightly smaller in BFO-400 °C than in BFO. FTIR spectra of the two samples are shown in Fig. 10(b). The bond vibrations of for Fe–O, Bi–O, nitro groups, and hydroxyl are almost the same for both BFO-400 °C and BFO. In addition, the Bi L_3-edge and Fe K-edge XAFS spectra of the two $BiFeO_3$ products are compared in Fig. 10(c) (also in Fig. S13, ESI†). The results demonstrate that the X-ray absorption curves of BFO-400 °C and BFO are almost overlapped, not only for the Bi L_3-edge, but also for the Fe K-edge, which implies that the two samples have very similar atomic neighbor structures. Further XAFS fittings, as shown in Fig. 10(d), verify that the near-neighbor structural parameters (Table S1, ESI†) are almost the same in both BFO-400 °C and BFO. These results demonstrate that the final $BiFeO_3$ products prepared by the calcination method or by hydrothermal synthesis have no obvious differences from the microstructural point of view.

4. Conclusion

In summary, the bismuth–iron-based precursor BFOH and other related precursors have been prepared. The precursor BFOH has been determined to be a mixture composed of $Bi_6O_6(NO_3)_4(OH)_2 \cdot 2H_2O$, $Bi_6O_5(NO_3)_5(OH)_3 \cdot 3H_2O$, α-Bi_2O_3, and $Fe(OH)_3$. As a precursor to synthesize $BiFeO_3$, the transformation of BFOH to $BiFeO_3$ was further studied under calcination treatment and hydrothermal synthesis. The mechanism of synthesizing the $BiFeO_3$ phase has been proposed and discussed, and the synthetic conditions optimized. The optimal calcination temperature to synthesize $BiFeO_3$ from the precursor BFOH is 400 °C. The optimal hydrothermal conditions include: a reaction time of 48 h, a preferred surfactant of CTAB, a hydrothermal temperature of 180 °C, and a concentration of KOH of at least 3 M. The two, as-prepared $BiFeO_3$ NPs prepared by calcination or hydrothermal synthesis have no notable differences from the point of view of microstructures.

Conflicts of interest

The authors declare no competing financial interest.

Acknowledgements

This work was supported by the National Key R&D Program of China (Grant No. 2017YFA0403000, and 2017YFA0403100) and the National Natural Science Foundation (No. U1232203) of China.

References

1 R. Safi and H. Shokrollahi, *Prog. Solid State Chem.*, 2012, **40**, 6–15.
2 H. Schmid, *Ferroelectrics*, 1994, **162**, 317–338.
3 G. Catalan and J. F. Scott, *Adv. Mater.*, 2009, **21**, 2463–2485.
4 M. S. Bernardo, *Bol. Soc. Esp. Ceram.*, 2014, **45**, 1–14.
5 T. Zhao, A. Scholl, F. Zavaliche, K. Lee, M. Barry, A. Doran, M. P. Cruz, Y. H. Chu, C. Ederer and N. A. Spaldin, *Nat. Mater.*, 2006, **5**, 823–829.
6 W. Prellier, M. P. Singh and P. Murugavel, *ChemInform*, 2006, **37**, R803.
7 D. Lebeugle, D. Colson, A. Forget, M. Viret, P. Bonville, J. F. Marucco and S. Fusil, *Phys. Rev. B: Condens. Matter Mater. Phys.*, 2007, **76**, 024116.
8 D. Yan, C. Sun, J. Jian, Y. Sun, R. Wu and J. Li, *J. Mater. Sci.: Mater. Electron.*, 2014, **25**, 928–935.
9 X. Wang, W. Mao, Q. Zhang, Q. Wang, Y. Zhu, J. Zhang, T. Yang, J. Yang, X. a. Li and W. Huang, *J. Alloys Compd.*, 2016, **677**, 288–293.
10 L. Zhang, X. F. Cao, Y. L. Ma, X. T. Chen and Z. L. Xue, *J. Solid State Chem.*, 2010, **183**, 1761–1766.
11 J. P. Zhou, R. J. Xiao, Y. X. Zhang, Z. Shi and G. Q. Zhu, *J. Mater. Chem. C*, 2015, **3**, 6924–6931.
12 S. Li, R. Nechache, C. Harnagea, L. Nikolova and F. Rosei, *Appl. Phys. Lett.*, 2012, **101**, 192903.
13 S. Li, J. Zhang, M. G. Kibria, Z. Mi, M. Chaker, D. Ma, R. Nechache and F. Rosei, *Chem. Commun.*, 2013, **49**, 5856.
14 B. Liu, B. Hu and Z. Du, *Chem. Commun.*, 2011, **47**, 8166–8168.
15 J. Varghese, R. W. Whatmore and J. D. Holmes, *J. Mater. Chem. C*, 2013, **1**, 2618.
16 X. Gang, Y. Yang, H. Bai, J. Wang, T. He, R. Zhao, W. Xiao, Y. Xin and G. Han, *CrystEngComm*, 2016, **18**, 2268–2274.
17 L. Xiaomeng, X. Jimin, S. Yuanzhi and L. Jiamin, *J. Mater. Sci.*, 2007, **42**, 6824–6827.
18 A. Chaudhuri, S. Mitra, M. Mandal and K. Mandal, *J. Alloys Compd.*, 2010, **491**, 703–706.
19 Z. Chen, W. Jin, Z. Lu and C. Hu, *J. Mater. Sci.: Mater. Electron.*, 2014, **26**, 1077–1086.
20 T. Gao, Z. Chen, F. Niu, D. Zhou, Q. Huang, Y. Zhu, L. Qin, X. Sun and Y. Huang, *J. Alloys Compd.*, 2015, **648**, 564–570.
21 S. H. Han, K. S. Kim, H. G. Kim, H. G. Lee, H. W. Kang, J. S. Kim and C. I. Cheon, *Ceram. Int.*, 2010, **36**, 1365–1372.
22 L. Hou, K. H. Zuo, Q. B. Sun, Z. M. Ren, Y. P. Zeng and X. Li, *Appl. Phys. Lett.*, 2013, **102**, 082901.
23 Z. C. Qiu, J. P. Zhou, G. Zhu, X. M. Chen, R. L. Yang and Y. H. Song, *J. Nanosci. Nanotechnol.*, 2012, **12**, 6552–6557.
24 C. Y. Song, J. Xu, A. Yimamu and L. Wang, *Integr. Ferroelectr.*, 2014, **153**, 33–41.
25 D. R. Modeshia and R. I. Walton, *Chem. Soc. Rev.*, 2010, **39**, 4303.
26 Y. Wang, G. Xu, L. Yang, Z. Ren, X. Wei, W. Weng, P. Du, G. Shen and G. Han, *J. Am. Ceram. Soc.*, 2007, **90**, 3673–3675.
27 X. Yang, G. Xu, Z. Ren, X. Wei, C. Chao, S. Gong, G. Shen and G. Han, *CrystEngComm*, 2014, **16**, 4176–4182.

28 R. V. Annapu, N. P. Pathak and R. Nath, *J. Alloys Compd.*, 2012, **543**, 206–212.
29 N. Das, R. Majumdar, A. Sen and H. S. Maiti, *Mater. Lett.*, 2007, **61**, 2100–2104.
30 H. Ke, W. Wang, Y. Wang, J. Xu, D. Jia, Z. Lu and Y. Zhou, *J. Alloys Compd.*, 2011, **509**, 2192–2197.
31 M. Y. Shami, M. S. Awan and R. M. Anis, *J. Alloys Compd.*, 2011, **509**, 10139–10144.
32 H. Shokrollahi, *Powder Technol.*, 2013, **235**, 953–958.
33 S. Ghosh, S. Dasgupta, A. Sen and H. S. Maiti, *Mater. Res. Bull.*, 2005, **40**, 2073–2079.
34 N. A. Lomanova and V. V. Gusarov, *Nanosyst.: Phys., Chem., Math.*, 2013, **4**, 696–705.
35 C. Paraschiv, B. Jurca, A. Ianculescu and O. Carp, *J. Therm. Anal. Calorim.*, 2008, **94**, 411–416.
36 J. Pang, Q. Han, W. Liu, Z. Shen, X. Wang and J. Zhu, *Appl. Surf. Sci.*, 2017, **422**, 283–294.
37 G. Backes, M. Sahlin, B. M. Sjöberg, T. M. Loehr and J. S. Loehr, *Biochemistry*, 1989, **28**, 1923.
38 V. Vivier, A. Régis, G. Sagon, J. Y. Nedelec, L. T. Yu and C. C. Vivier, *Electrochim. Acta*, 2002, **46**, 907–914.
39 Z. Ai, Y. Huang, S. Lee and L. Zhang, *J. Alloys Compd.*, 2011, **509**, 2044–2049.
40 L. Liu, J. Jiang, S. Jin, Z. Xia and M. Tang, *CrystEngComm*, 2011, **13**, 2529.
41 J. Laane and J. R. Ohlsen, *Prog. Inorg. Chem.*, 1986, **28**, 465–509.
42 I. L. Schneider, E. C. Teixeira, D. M. A. Castaneda, E. S. G. Silva, N. Balzaretti, M. F. Braga and L. F. S. Oliveira, *Sci. Total Environ.*, 2016, **541**, 1151–1160.
43 S. Ghosh, S. Dasgupta, A. Sen and H. Sekhar Maiti, *J. Am. Ceram. Soc.*, 2005, **88**, 1349–1352.
44 C. Wang, Q. Liu and Z. Li, *Cryst. Res. Technol.*, 2011, **46**, 655–658.
45 R. Kefirov, E. Ivanova, K. Hadjiivanov, S. Dzwigaj and M. Che, *Catal. Lett.*, 2008, **125**, 209–214.
46 B. Ravel and M. Newville, *J. Synchrotron Radiat.*, 2005, **12**, 537–541.
47 H. A. Harwig, *Z. Anorg. Allg. Chem.*, 1978, **444**, 151–166.
48 S. K. Blower and C. Greaves, *Acta Crystallogr.*, 2014, **44**, 587–589.
49 J. Wei, C. Zhang and Z. Xu, *Mater. Res. Bull.*, 2012, **47**, 3513–3517.
50 Y. Wu, Q. Han, L. Wang, X. Wang and J. Zhu, *Mater. Chem. Phys.*, 2017, **187**, 72–81.
51 Z. Chen and W. Jin, *J. Mater. Sci.: Mater. Electron.*, 2014, **25**, 4039–4045.
52 Y. Liu, L. Qian, X. Zhao, J. Wang, L. Yao, X. Xing, G. Mo, Q. Cai, Z. Chen and Z. Wu, *CrystEngComm*, 2019, **21**, 2799–2808.
53 Q. Wang, T. Hisatomi, Q. Jia, H. Tokudome, M. Zhong, C. Wang, Z. Pan, T. Takata, M. Nakabayashi, N. Shibata, Y. Li, I. D. Sharp, A. Kudo, T. Yamada and K. Domen, *Nat. Mater.*, 2016, **15**, 611–615.
54 Y. He, Y. Zhang, H. Huang, N. Tian and Y. Luo, *Inorg. Chem. Commun.*, 2014, **40**, 55–58.
55 V. Annapu Reddy, N. P. Pathak and R. Nath, *J. Alloys Compd.*, 2012, **543**, 206–212.
56 W. Ji, M. Li, G. Zhang and P. Wang, *Dalton Trans.*, 2017, **46**, 10586–10593.
57 Y. Liu, R. Zuo and S. Qi, *Powder Technol.*, 2014, **254**, 30–35.
58 M. S. Bernardo, T. Jardiel, M. Peiteado, A. C. Caballero and M. Villegas, *J. Eur. Ceram. Soc.*, 2011, **31**, 3047–3053.
59 L. Wang, J. B. Xu, B. Gao, A. M. Chang, J. Chen, L. Bian and C. Y. Song, *Mater. Res. Bull.*, 2013, **48**, 383–388.
60 H. Yang, X. Zhang, W. Ao and G. Qiu, *Mater. Res. Bull.*, 2004, **39**, 833–837.
61 M. G. Scott, *Amorphous Metallic Alloys*, Butterworths, London,1983.
62 S. M. Selbach, M. A. Einarsrud, T. Tybell and T. Grande, *J. Am. Ceram. Soc.*, 2007, **90**, 3430–3434.
63 J. Huang, G. Tan, W. Yang, L. Zhang, H. Ren and A. Xia, *Mater. Sci. Semicond. Process.*, 2014, **25**, 84–88.
64 X. Wang, W. Mao, Q. Zhang, Q. Wang, Y. Zhu, J. Zhang, T. Yang, J. Yang, X. Li and W. Huang, *J. Alloys Compd.*, 2016, **677**, 288–293.
65 B. H. Toby, *J. Appl. Crystallogr.*, 2001, **34**, 210–213.